

Research Article

Influence of Flaw Inclination Angle on Unloading Responses of Brittle Rock in Deep Underground

Zhenghong Chen ¹, Xibing Li ¹, Lei Weng ², Shaofeng Wang ¹ and Longjun Dong ¹

¹School of Resources and Safety Engineering, Central South University, Changsha 410083, China

²School of Civil Engineering, Wuhan University, Wuhan 430072, China

Correspondence should be addressed to Xibing Li; xbli@csu.edu.cn

Received 11 July 2018; Revised 4 November 2018; Accepted 4 December 2018; Published 13 February 2019

Guest Editor: Mandadige S. A. Perera

Copyright © 2019 Zhenghong Chen et al. This is an open access article distributed under the Creative Commons Attribution License, which permits unrestricted use, distribution, and reproduction in any medium, provided the original work is properly cited.

Excavation unloading is a primary stress condition for engineering rock mass in deep underground. Based on the unloading stress condition during the excavation operation, this paper employed a distinct element method (DEM) to simulate the unloading responses of intact and preflawed rock specimens. The simulation results revealed that the unloading failure strength, unloading damage thresholds, and cracking characteristics were largely dependent on the inclination angle (α) of the preflaws. With the increase in the flaw inclination angle, the unloading failure strength of a preflawed specimen exhibited a sigmoidal curve increasing trend, and it decreased by 5.5%-20% compared to the unloading failure strength of an intact specimen. Based on the crack accumulation in specimens, three damage thresholds were identified under unloading condition and two damage thresholds σ_{ci} and σ_{di} were found to be increased with the increase in the flaw inclination angle. Furthermore, when the flaw inclination angle was smaller, cracks were initiated around the preflaws, and there were obvious axial splitting cracks in the failure modes of preflawed specimens, while axial splitting cracks were few in the preflawed specimen with a larger flaw inclination angle and none in the intact specimen. These unloading responses indicate that inducing preflaws can reliably reduce the unloading failure strength and promote the cracking process of hard rock during an excavation unloading process. Moreover, inducing preflaws with a smaller inclination angle (e.g., vertical to the unloading direction) will be more helpful for the unloading failure and rock cracking during an excavation unloading process.

1. Introduction

With the increasing demand of minerals and energy resources, mining operations and other resource excavations turned to deep underground. In deep underground operations or excavations, the construction environment is complex, usually involving high in situ stress, high geotemperature, and high water pressure [1–3]. The excavation activities may induce an important effect on the deformation and failure of rock mass in such complex environment. Particularly, when the drill-and-blast method is used in deep underground excavations, the high in situ stress in the horizontal direction is unloaded instantly, accompanied by a stress concentration in the vertical direction. In this process, the transient released strain energy dissipates completely in the rock mass [4]. Therefore, the underground

mining may lead to sudden and severe rock mass failure, posing a significant threat to the safety and stability of underground structures [5–7]. In this regard, the mechanical excavation method with controllable energy release is considered to be superior to the drill-and-blast method in the operations of underground excavation such as mining and tunneling [8]. Nowadays, mining equipment manufacturers are developing new machine concepts with the aim of using a mechanical excavation method in underground mining and tunneling operations [9]. However, the applications of mechanical cutting and excavation tools (e.g., road headers and tunnel boring machines (TBMs)) are limited due to the high strength and high integrity of the hard rock. Particularly in underground deep mining, it has been clearly demonstrated that high rock strength and integrity will significantly influence the excavation performance of road

headers [10] and TBMs [11, 12]. Therefore, by reducing the rock strength and integrity, it would be possible that the small and flexible continuous excavation machine can perform well in hard rock underground excavation.

One of the simplest and most straightforward ways of reducing rock strength and integrity on purpose is to induce preflaws in the hard rock. Over the last few years, extensive studies have been conducted to investigate the mechanical behavior of rock materials containing preflaws. For instance, Yang and Jing [13], Li et al. [14], and Zhang et al. [15] explored the cracking behavior of rock containing preexisting flaws, and the influences of different flaw geometries (flaw inclination angle, flaw length, and flaw size) on the rock failure were discussed. Bi et al. [16] studied the effect of confining pressure on failure behaviors of preflawed rock specimens, and the results indicated that the growth of tensile cracks and wing cracks was restrained with the increase in confining pressure. Lee and Jeon [17] discussed the fracture coalescence of three different preflawed materials (i.e., PMMA, molded gypsum, and granite) and summarized the common and different features of the cracking process depending on the materials. Zhuang et al. [18] and Park and Bobet [19] comparatively investigated the different mechanisms of crack coalescence between open and closed flaws, and they found that the peak stress and initiation and coalescence stresses for closed flaws were higher than those for open flaws. Huang et al. [20] conducted experiments on sandstones with two preexisting flaws; the results show that the arrangement of the flaw pair and the confining pressure have remarkable impacts on the deformation, strength, and crack coalescence pattern of rock. These investigations revealed that the flaws in rock played a significant role in the cracking and failure behavior of rock material. However, the fracturing and failure behavior of preflawed rock in previous studies were obtained from uniaxial or biaxial compression conditions, in which the fracturing and failure characteristics of preflawed rock under excavation unloading condition have not been involved.

Under unloading condition, both experimental and numerical investigations have been performed to study the mechanical responses of rock materials. For example, Zhao et al. [21] investigated the influence of the unloading rate on strain burst under unloading conditions, and they found that granite was more prone to occur strain burst with a higher unloading rate. Huang and Li [22] conducted unloading tests on marbles, and the results indicated that higher initial confining pressure and unloading rate will result in severer “flying fragment” phenomenon. Du et al. [23] investigated the unloading behavior of granite, red sandstone, and cement mortar, showing that slabbing occurred in the granite and sandstone specimens, whereas typical shear failures were observed in the cement mortar samples. Zhao and He [24] investigated the effects of granite size on its unloading behavior; they found that the rock strength exhibits an increasing trend with the decrease in a height-to-thickness ratio. Manouchehrian and Cai [25] performed a series of numerical studies to explore the effects of loading system stiffness, aspect ratio of a specimen, and intermediate principal stress on the unloading failure behavior of granite model

specimens. The associated simulation results showed that low-stiffness loading system, tall specimen, and low intermediate principle stress could induce violent unloading failure. In addition, Li et al. [26] presented a theoretical solution to obtain the stress state of highly stressed rock under quasi-static and intensive unloading conditions and found that the initial stress was a critical factor that governs the rock failure. So far, most of the previous studies concerning the unloading responses were performed on intact rock specimens, while the differences in the unloading responses between intact rock and preflawed rock are unclear.

In recent years, the numerical method plays an important role in researches related to rock materials [27–29]. For example, the distinct element method (DEM) provides an efficient access to characterize the mechanical behavior of brittle rocks. Compared with laboratory tests, using DEM to investigate the unloading failure behavior of preflawed rocks has the following superiorities: (1) apart from the variation of the flaw inclination angle, the preflawed numerical specimen is exactly identical, eliminating the disturbances of the geometrical errors of induced preflaws or the material heterogeneities of rock specimen in laboratory experiments; (2) all the numerical data are accessible at any arbitrarily instantaneous moment during the unloading process; and (3) the cracking process of rocks involving the initiation, propagation, and coalescence can be explicitly exhibited. Moreover, the numerical simulation is highly efficient, repeatable, and low-cost.

In the present study, the unloading failure responses of intact and preflawed rocks in the excavation unloading process are systematically investigated by DEM. First, the fundamentals of DEM are briefly introduced. Then, the unloading stress condition during excavation operations is analyzed, followed by a detailed simulation description of the unloading process on rock specimen, involving the calibration of an intact specimen, the induction of preflaws, and the reproduction of an unloading stress path. Finally, the unloading responses including unloading failure strength, damage thresholds, and cracking process were investigated with the consideration of the effect of the preflaws.

2. Brief Description of DEM

The DEM-based software particle flow code (PFC) is employed to investigate the unloading behavior of a rock specimen. In the DEM model, the rock specimen is simulated as an assembly of densely packed and bonded rigid spherical particles, in which two adjacent particles are cemented together by a bond (see Figure 1). The mechanical properties of the model are controlled by the microparameters of particles and bonds [30]:

$$\left\{ E_c, \left(\frac{k^n}{k^s} \right), \mu \right\}, \quad \text{particle microparameters,} \quad (1)$$

$$\left\{ \bar{E}_c, \left(\frac{\bar{k}^n}{\bar{k}^s} \right), \bar{\lambda}, \bar{\sigma}_c, \bar{\tau}_c \right\}, \quad \text{bond microparameters,}$$

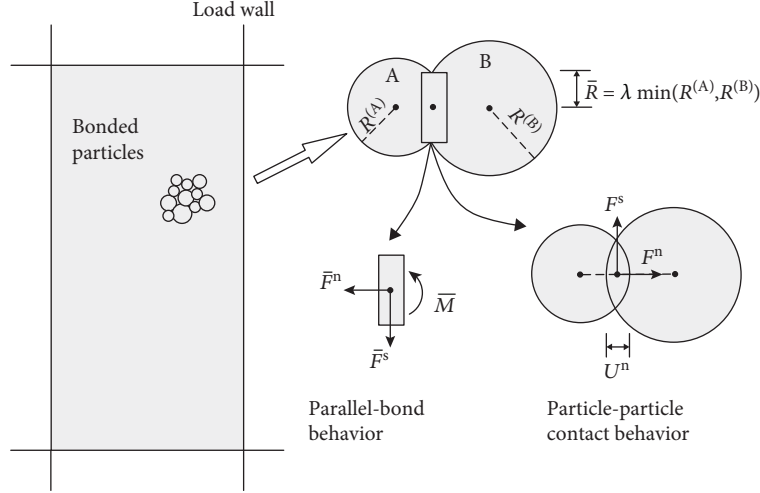


FIGURE 1: Sketch map of the bond particle model.

where E_c and \bar{E}_c are Young's moduli of the particles and bonds, respectively, (k^n/k^s) and (\bar{k}^n/\bar{k}^s) are the ratios of normal-to-shear stiffness of the particles and bonds, respectively, $\bar{\lambda}$ is the ratio multiplier of a parallel bond, μ is the particle friction coefficient, and $\bar{\sigma}_c$ and $\bar{\tau}_c$ are the tensile and shear strengths of the bonds, respectively.

The mechanical behavior of the particle-bond system consisted of the particle-particle contact behavior and the parallel-bond behavior. The normal force F^n in the particle-particle contact behavior is calculated by

$$F^n = k^n U^n, \quad (2)$$

where U^n is the overlap between particles and k^n is the normal stiffness of the particles.

The shear force F^s is computed in an incremental fashion. When the contact is formed, F^s is initialized to zero. Each subsequent shear-displacement increment (ΔU^s) will result in an increment of shear force:

$$\Delta F^s = -k^s \Delta U^s. \quad (3)$$

The normal force \bar{F}^n , shear force \bar{F}^s , and the bending moment \bar{M} in the parallel-bond behavior are also computed in an incremental fashion:

$$\begin{aligned} \Delta \bar{F}^n &= \bar{k}^n A \Delta U^n, \\ \Delta \bar{F}^s &= -\bar{k}^s A \Delta U^s, \\ \Delta \bar{M} &= -\bar{k}^n I \Delta \theta^s, \end{aligned} \quad (4)$$

where ΔU^n , ΔU^s , and $\Delta \theta^s$ are the subsequent displacement and rotation increments and A and I are the area of bond across section and the moment of inertia, respectively.

The following breakage criterion of the model is employed in this study:

$$\begin{aligned} \frac{\sigma_{\max}}{\bar{\sigma}_c} &\geq 1, \\ \frac{\tau_{\max}}{\bar{\tau}_c} &\geq 1, \end{aligned} \quad (5)$$

where σ_{\max} and τ_{\max} denote the maximum tensile stress and maximum shear stress, respectively, and they are calculated from

$$\begin{aligned} \sigma_{\max} &= \frac{-\bar{F}^n}{A} + \frac{|\bar{M}|}{I} \bar{R}, \\ \tau_{\max} &= \frac{|\bar{F}^s|}{A}, \end{aligned} \quad (6)$$

where \bar{R} is the bond radius. These calculation equations have received wide acceptance to simulate the fracture mechanism of rocks [31, 32].

3. Unloading Description

3.1. Unloading Stress Condition. Uniaxial, biaxial, and triaxial compression tests are often performed to investigate rock mechanical property and behavior, whereas the stress conditions of these compression tests are quasi-static loading, and none of them can reflect the in situ stress variation process of rock mass during excavation [33]. In order to better understand the unloading process of in situ stress during the excavation operations, the stress condition of excavation unloading is analyzed.

During the excavation process, the stress distribution of rock masses ahead of the working face is shown in Figure 2, where σ_z is the vertical stress, σ_x is the horizontal stress, p_0 is the in situ geostress, x is the distance between the working face and rock mass, z is the height from the tunnel center, and R represents a rock mass unit ahead of the working face. As illustrated in Figure 2, the rock masses ahead of the

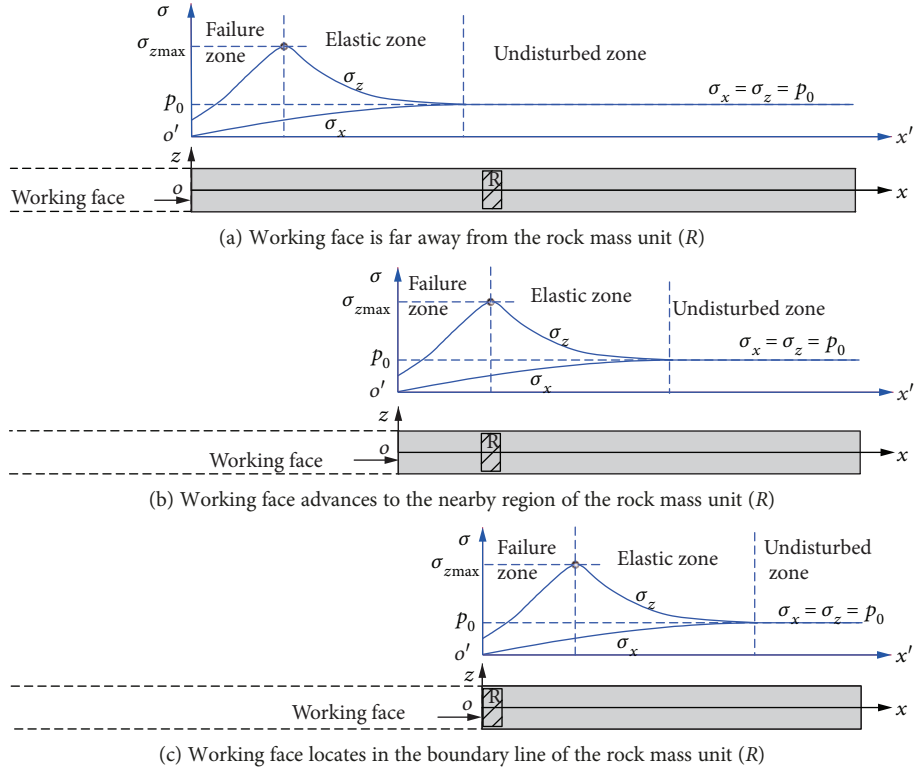


FIGURE 2: Stress distribution of rock mass ahead of the working face.

working face can be divided into three zones: undisturbed zone, elastic zone, and failure zone. Rock mass in the undisturbed zone is under an in situ stress condition. Rock mass in the elastic zone is under an elastic deformation condition, while the rock mass in the failure zone is damaged. With the advancing of the working face, the stress distribution ahead of the working face also moves forward (as shown in Figures 2(a)–2(c)). Therefore, for the rock mass unit (R) in an underground engineering which is ready for excavation, it will undergo three stages of stress states during the advance process of the working face (Figure 3). When the excavation is just starting and the working face is far away from the rock mass unit ($0 \leq t < t_0$), the rock mass unit is under a hydrostatic in situ stress state; with the advancing of the working face, the horizontal in situ stress on it is unloaded or released, accompanied by an increase in the vertical in situ stress ($t_0 \leq t < t_p$); when the working face advances to the vicinity area of the rock mass unit, the rock failure will happen ($t_p \leq t < t_n$). During the advance process of the working face, the variation process of horizontal in situ stress can be given by

$$\sigma_x = \begin{cases} p_0, & 0 \leq t < t_0, \\ p_0 f(t), & t_0 \leq t \leq t_n, \end{cases} \quad (7)$$

where $f(t)$ is a decreasing function and represents the unloading path of horizontal in situ stress, and different excavation methods will induce different unloading paths.

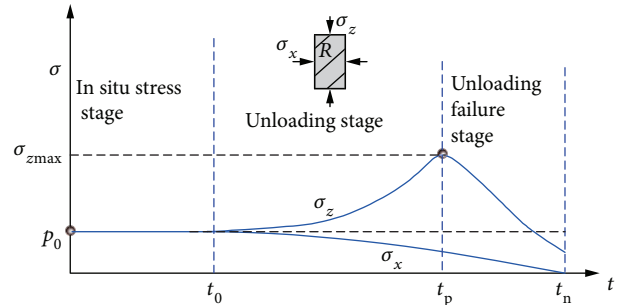


FIGURE 3: Stress variation of the rock mass unit (R) with the advancing of the working face, and t is the time of the stress variation process.

The variation process of the vertical in situ stress is a stress concentration failure process, and it will reach a peak stress before the rock failure. The peak stress can be written as

$$\sigma_{z \max} = \sigma_{z/t=t_p} = k p_0, \quad (8)$$

where k is the stress concentration factor, and the value of k depends on the unloading process of horizontal in situ stress.

Such stress variation processes are the practical stress condition that rock mass will undergo during the excavation in high geostress, which are defined as the unloading process. In this study, the mechanical response of a preflawed rock specimen under such unloading process is investigated, in

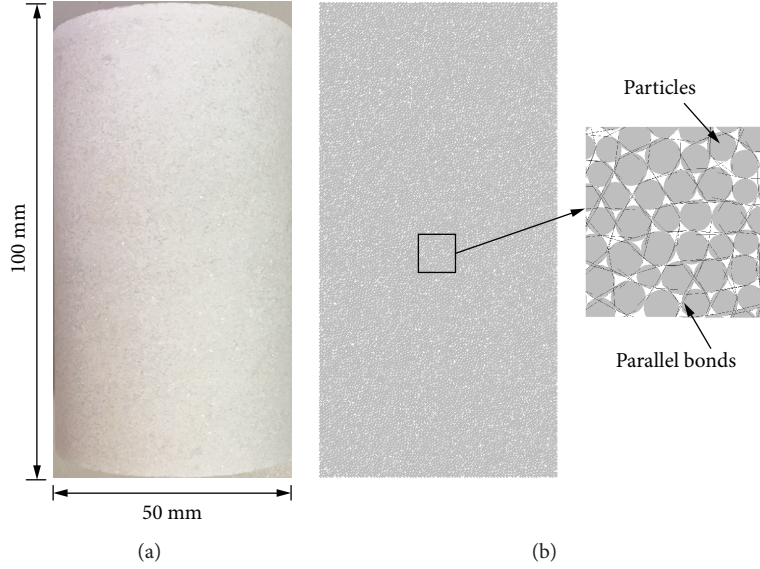


FIGURE 4: Intact marble specimens.

TABLE 1: Microparameters of the numerical specimen.

Particle microparameters		Bond microparameters	
Minimum radius R_{\min} (mm)	0.25	Parallel bond modules \bar{E}_c (GPa)	58
Particle size ratio R_{\max}/R_{\min}	1.5	Tensile strength $\bar{\sigma}_c$ (MPa)	94 ± 5
Contact modules E_c (GPa)	58	Shear strength $\bar{\tau}_c$ (MPa)	188 ± 5
Frictional coefficient μ	0.65	Stiffness ratio \bar{k}^n/\bar{k}^s	2.5
Stiffness ratio k^n/k^s	2.5	Ratio multiplier $\bar{\lambda}$	1.0

order to understand the unloading failure mechanism of rock mass containing preflaws.

3.2. Numerical Specimen. In order to numerically reproduce the unloading process of rock material, it is critical to establish a suitable numerical model which can reproduce the mechanical behavior of rock. The rock material for investigation is called ‘‘Leiyang white’’ marble, which was collected from Leiyang City in China. The marble has a connected porosity of approximately 0.56% and an average density of 2810 kg/m^3 . The mechanical behaviors of the marble were obtained through a laboratory uniaxial compression test and triaxial compression test at 40 MPa confining pressure. In laboratory tests, all the marble specimens were cored from an identical block to minimize the scatter effect, and specimens were prepared with dimensions of 50 mm in diameter and 100 mm in height following the ISRM-suggested method [34] (Figure 4(a)). The tests were conducted using the MTS 815 rock mechanics system in the Advanced Research Center at Central South University. The specimens were loaded till failure occurs under a displacement control module, and the loading rate is 0.15 mm/min.

The numerical model was established with the same size as the marble specimen (Figure 4(b)). Through adjusting the values of microparameters (as in equation (1)) in the numerical model, a series of uniaxial compression tests and triaxial

compression tests at 40 MPa confining pressure were numerically simulated. In the uniaxial compression numerical test, the specimen was placed between the top and bottom load walls. The loading rate of load walls was set to 0.05 m/s. In the numerical triaxial compression test, the specimen was surrounded by four load walls. The confining pressure applied to the two lateral walls was set to a constant value of 40 MPa, and the loading rate for top and bottom walls was 0.05 m/s. After a series of trial and error, a suitable set of microparameters (Table 1) was obtained to establish the numerical marble specimen which can reproduce the mechanical behavior of the real marble specimen.

Table 2 shows the comparisons of the macromechanical behavior of marble specimens from laboratorial and numerical tests. In Table 2, UCS is the uniaxial compression strength and TCS-40 refers to triaxial compression strength at confining pressures of 40 MPa. It is seen that the mechanical properties of numerical marble specimens are much close to those of real marble specimens. Therefore, the established numerical marble specimen commendably reproduced the mechanical properties of the real marble specimen. Figure 5 shows the comparison of laboratorial and numerical stress-strain curves of the marble specimen. From Figure 5, it can be seen that the numerical curves under compression tests agree well with the laboratorial curves, including the crack initiation and growth stage before the peak strength and the

TABLE 2: Laboratorial and numerical macromechanical behavior of the marble specimen.

	Experimental results	Numerical results	Errors (%)
Density (g/cm^3)	2.81	2.81	—
Young's modulus (GPa)	76.4	75.6	1.05
Poisson's ratio	0.21	0.21	—
UCS (MPa)	135.3	136.1	0.59
TCS-40 (MPa)	273.5	264.2	3.40

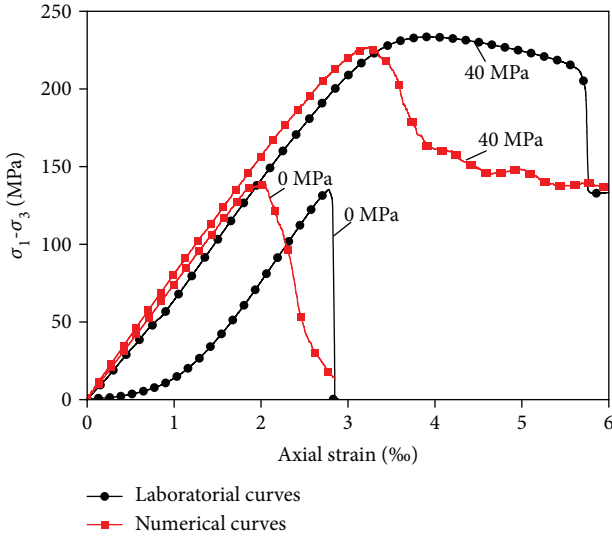


FIGURE 5: Laboratorial and numerical stress-strain curves of the marble specimen under compression.

unstable failure stage after the peak strength. However, the numerical curve does not mirror the initial nonlinearity deformation (crack closure stage) in the uniaxial compression test. This is because the real rock specimen generally contains natural microfractures while the numerical rock specimen consisted of a compacted assembly of rigid particles. Moreover, the numerical curve does not show the postpeak strain softening in the triaxial compression test at 40 MPa confining pressure. Nevertheless, the discrepancies in the nonlinearity deformation and the postpeak strain softening between the numerical and laboratorial curves do not cause large differences of failure modes. As shown in Figure 6, the failure mode of the numerical marble specimen in the uniaxial compression test showed a typical splitting failure, and the failure mode in the triaxial compression test is in a shear fashion. These failure modes are highly consistent with those obtained in laboratory. The comparisons presented in Table 2 and Figures 5 and 6 justified that the calibrated numerical marble specimen has the capability of simulating the mechanical behavior of the marble.

After establishing the suitable intact numerical marble specimen, preflaws were created in the numerical specimen to investigate the influence of the flaw inclination angle on unloading responses. Technologies under consideration for

inducing preflaws in real underground rock include thermal perturbation, high-pressure water jet, and high-power microwaves. These technologies use different damage mechanisms to generate flaw networks in the rock. For simplification, in this study, just two straight flaws were added at the center of the numerical specimen. The geometry of the two flaws in the numerical marble specimens is shown in Figure 7. The flaw length (L_1) is 10 mm, and the bridge length between the flaws (L_2) is 14 mm. The bridge angle (β) is 30° , and the flaw inclination angle (α) varies from 0° to 90° in 30° interval. The flaws were created by deleting particles in a specific range. Since the particles in the model cannot be divided, the surfaces of the induced flaws are not smooth as can be observed in Figure 7.

3.3. Unloading Procedure. During the drill-and-blast excavation, the release of in situ stress is a transient process. While during the mechanical excavation, the unloading of in situ stress is a quasi-static process [35, 36]. In the present study, to analyze the quasi-static unloading process during the mechanical excavation, the typical stress condition of the quasi-static unloading process as illustrated in Section 3.1 was simulated by varying the boundary stresses on the rock specimens. To this end, a set of self-defined functions was encoded in the PFC program. The procedures for the unloading simulation were presented in detail as follows:

Step 1 ($0 \leq t < t_0$). Increase the lateral pressure (σ_3) to the in situ stress level, and simultaneously load the axial pressure (σ_1) to the in situ stress level; then, keep them unchanged for a while.

Step 2 ($t_0 \leq t < t_p$). Unload the lateral pressure (σ_3), while the axial pressure (σ_1) increases at a specified rate until the peak stress ($\sigma_{1 \max}$).

Step 3 ($t_p \leq t \leq t_n$). After the peak stress of the specimen, the lateral pressure (σ_3) is unloaded continuously to zero to finish the unloading, while the axial pressure (σ_1) will decrease spontaneously due to the failure of the specimen.

To eliminate the unloading wave effect and to keep a quasi-static unloading process, a high-damp parameter was adopted in the modelling. The axial pressure (σ_1) was applied in a displacement-controlled manner at a rate of 0.05 m/s. Through recoding the servo-controlled program, the lateral pressure was unloaded in a linear form following

$$\sigma_3 = \begin{cases} p_0, & 0 \leq t < t_0, \\ p_0 \left(1 - \frac{t - t_0}{t_n - t_0}\right), & t_0 \leq t \leq t_n, \end{cases} \quad (9)$$

where p_0 is the in situ stress level, initially set as 40 MPa; t is the unloading time; t_0 is the initiation moment of unloading, set as 1 ms; t_n is the end moment of the unloading process, set as 3 ms. Therefore, the unloading period in the simulation was 2 ms. During the numerical simulation process in DEM, a critical and reasonable time

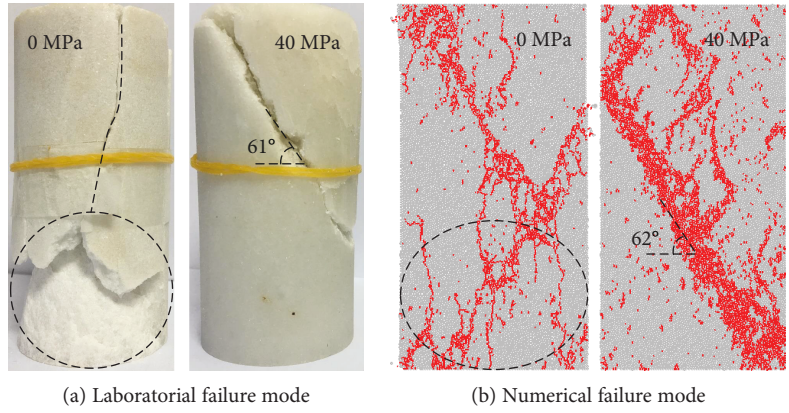


FIGURE 6: Laboratorial and numerical failure modes of marble specimens under compression (the red short lines in numerical specimens represent microcracks).

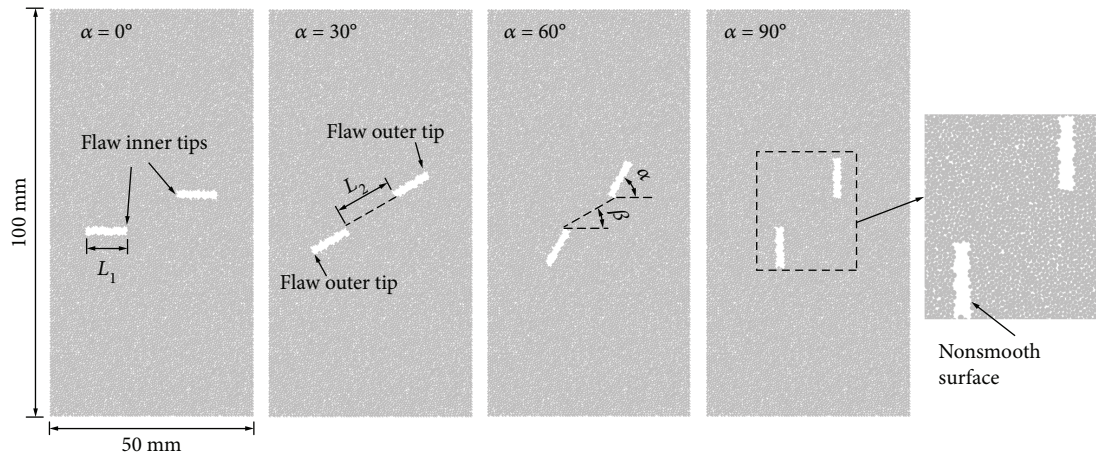


FIGURE 7: Numerical marble specimens containing two preflaws.

step was internally assigned in the program before each program cycle. The time step for the current simulation is merely about 2.2×10^{-8} s/step; thus, the unloading rate of the lateral pressure can be translated to 4.4×10^{-4} MPa/step, while the loading rate of the axial pressure can be translated to 1.1×10^{-6} mm/step. Such unloading and loading rates are low enough to simulate the quasi-static unloading process similar to the tunnel excavation with a mechanical method.

4. Simulation Results and Discussions

In an underground mechanical excavation process, the rock mass undergoes the unloading process caused by stress redistribution before subjecting to the cutting force of machines. If the rock failure happens during the unloading process, the cutting using an excavation machine will be easier, and it will be helpful to improve the excavation efficiency. This means that the unloading of minimum principal stress and the concentration of maximum stress throughout the unloading process greatly affect the subsequent cutting process of

excavation machines. Therefore, it is important to investigate the failure behavior of rock mass during the unloading process. In this section, the failure behavior of intact and preflawed specimens during the unloading process will be discussed in detail.

4.1. Unloading Failure Strength of Preflawned Specimens. The stress variations against time for the specimens during unloading simulations are shown in Figure 8. It can be found that the specimens experience the typical three stress stages which have been specified in Section 3.1. At first, the specimen was under a hydrostatic pressure state for 1 ms. Then, the lateral stress (σ_3) was unloaded and the axial stress (σ_1) increased to a peak value. Finally, the specimen underwent the unloading failure stage, in which the lateral stress (σ_3) was unloaded to zero and the axial stress (σ_1) dropped due to specimen failure. The peak stress (σ_1) was defined as unloading failure strength (σ_{us}). Note that the unloading failure strength is different from the failure strength in the conventional compression test, which is the actual failure strength for rock mass during the excavation process.

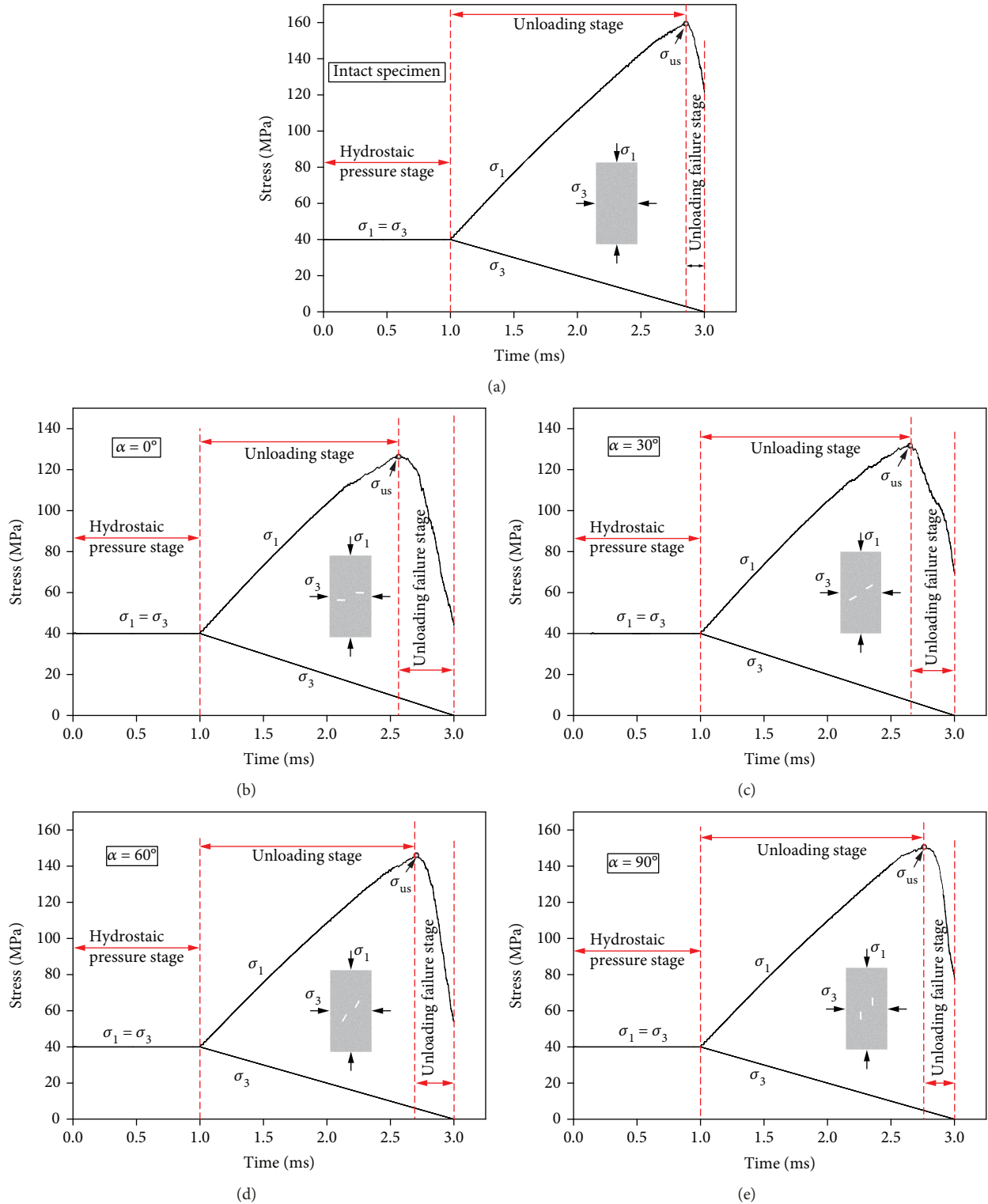


FIGURE 8: Stress–time curves of specimens under unloading condition.

It is seen in Figure 8 that the unloading failure strength varies significantly for different specimens depending on the geometry of the specimen. For the intact specimen, the unloading failure strength is greater than that for the preflawed specimen. Furthermore, an increase in the

unloading failure strength can be observed for the preflawed specimen with the increase in the flaw inclination angle. In order to better understand the influence of preflaws on the strength properties of rock specimens under unloading condition, quantitative investigations on

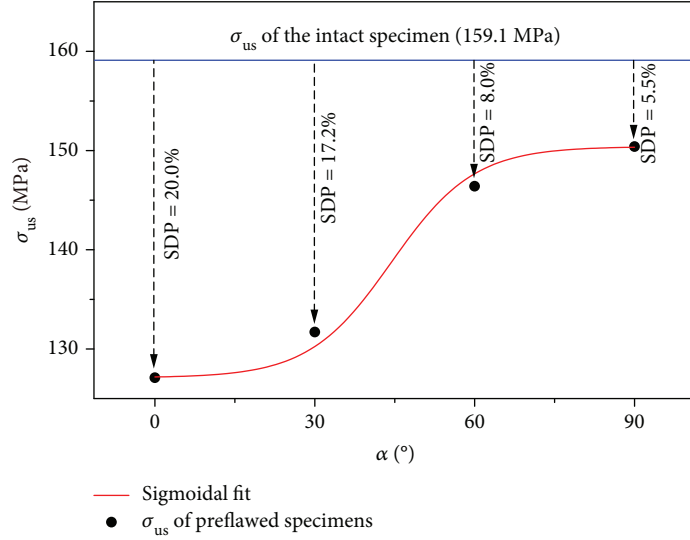


FIGURE 9: Unloading failure strength (σ_{us}) of preflawed specimens.

the unloading failure strength were carried out. Figure 9 presented the correlation between the unloading failure strength and flaw inclination angle. In addition, the strength degradation parameter (SDP) was introduced to compare the unloading failure strength characteristics of the preflawed specimen and intact specimen. The SDP is defined as

$$SDP = \left(\frac{\Delta\sigma_{us}}{\sigma_{usi}} \right) \times 100\% = \left[\frac{\sigma_{usi} - \sigma_{usf}}{\sigma_{usi}} \right] \times 100\%, \quad (10)$$

where σ_{usi} is the unloading failure strength of the intact specimen and σ_{usf} is the unloading failure strength of the preflawed specimen under the same unloading condition.

The SDP values can show the reduction degrees of the unloading failure strength of preflawed marble specimens relative to that of the intact marble specimen. The SDP values of the preflawed specimens with various flaw inclination angles indicate that the unloading failure strengths of the preflawed specimens decrease by 5.5%–20% compared with those of the intact specimen. Such phenomena indicate that the existence of preflaws in the rock mass can reliably decrease the unloading failure strength. Therefore, inducing preflaws in intact hard rock is helpful to cause rock failure during the unloading process and to improve the cutting efficiency.

As shown in Figure 9, the unloading failure strength of the preflawed specimen exhibits an “S”-shape rising trend with the increase in the flaw inclination angle. This means that the preflaws with a smaller inclination angle can reduce the unloading failure strength to a greater extent. Previous studies also showed that the strength of the preflawed specimen was closely dependent on the inclination angle of flaws [37, 38]. To further explain the influences of preflaws on the unloading failure strength, the stress state on the flaws was theoretically analyzed. The stress state sketch of preflaws under unloading condition is shown in Figure 10. The

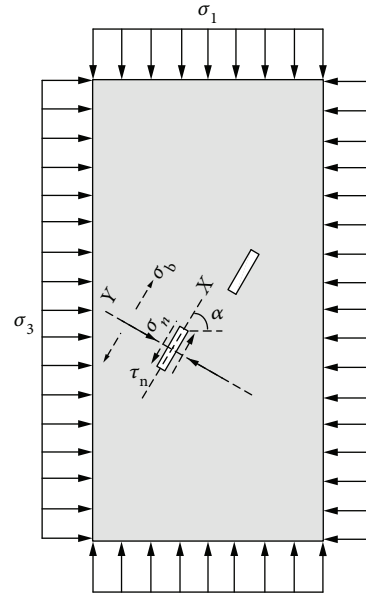


FIGURE 10: Stress state sketch of preflaws.

normal stress σ_n and the shear stress τ_n on the flaw surface can be expressed as

$$\begin{aligned} \sigma_n &= \sigma_1 \cos^2\alpha + \sigma_3 \sin^2\alpha, \\ \tau_n &= \frac{\sigma_1 - \sigma_3}{2} \sin 2\alpha, \end{aligned} \quad (11)$$

where α is the inclination angle of flaw and σ_1 and σ_3 are the axial pressure and lateral pressure, respectively. It should be noted that the flaws are open and the normal stress (σ_n) on the flaw can induce tensile stress (σ_b).

The normal stresses (σ_n) and shear stresses (τ_n) on the flaws with the four different inclination angles can be calculated by substituting $\alpha = 0^\circ, 30^\circ, 60^\circ,$ and 90° into equation

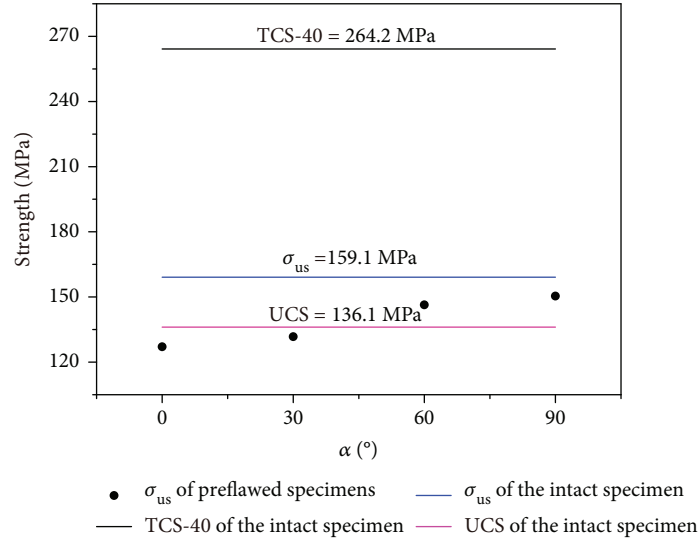


FIGURE 11: Comparisons of the unloading failure strength (σ_{us}) and the compressive strength (UCS, TCS-40).

(11). It is known that the cracking of the rock material usually presents two forms: tensile cracking or shear cracking. If the extreme value of the tensile or shear stress appears and satisfies the tensile or shear strength, then the tensile cracking or shear cracking will happen. For the brittle rock specimen, the tensile strength is much smaller than the shear strength, and the tensile stress plays a dominate role in the cracking of the rock specimen. Comparing the calculated results in equation (11) for flaws with inclination angles of 0° , 30° , 60° , and 90° , it can be found that for the flaw with $\alpha = 0^\circ$, its shear stress is zero ($\tau_{n(0^\circ)} = 0$) and its normal stress is much larger than that of flaws with other inclination angles ($\sigma_{n(0^\circ)} = \sigma_1$, $\sigma_{n(0^\circ)} > \sigma_{n(30^\circ)} > \sigma_{n(60^\circ)} > \sigma_{n(90^\circ)}$). Thus, the induced tensile stress ($\sigma_{b(0^\circ)}$) is the largest and tensile cracks are most likely to initiate and propagate around the flaws, hence resulting in the lowest unloading failure strength. For flaws with $\alpha = 30^\circ$ and $\alpha = 60^\circ$, they suffer nearly the same shear stresses ($\tau_{n(30^\circ)} \approx \tau_{n(60^\circ)}$); however, the flaw with $\alpha = 30^\circ$ suffers a larger normal stress than the flaw with $\alpha = 60^\circ$. Therefore, the induced tensile stress on the flaw with $\alpha = 30^\circ$ is larger ($\sigma_{b(30^\circ)} > \sigma_{b(60^\circ)}$), which means that it is more likely to initiate cracks around the flaw with $\alpha = 30^\circ$, and it may result in a lower failure strength for the preflawed specimen with $\alpha = 30^\circ$. For flaws with $\alpha = 90^\circ$, their shear stress is zero ($\tau_{n(90^\circ)} = 0$) and their normal stress is the smallest ($\sigma_{n(90^\circ)} = \sigma_3$). In this regard, the normal stress is decreasing and it is not great enough to initiate cracks around the flaw. Thus, the failure of the specimen with a flaw inclination angle of 90° is not significantly affected by the flaw, and this is the reason why its unloading failure strength is close to the strength of the intact specimen. These findings indicate that if we induce preflaws with a smaller inclination angle in the specimen (i.e., vertical to the unloading direction), cracks are more likely to initiate and propagate around the flaws and the failure of the specimen is more easily to happen. Therefore, during the unloading process, preflaws

with a smaller inclination angle can result in the failure of the specimen that happens more easily.

Figure 11 shows the comparison between the unloading failure strength and compression failure strength of specimens. It can be seen that the unloading failure strength of the intact specimen is merely 60% of the triaxial compressive strength of the intact specimen, which is, however, approximately 1.2 times the UCS of the intact specimen. Meanwhile, the average value of the unloading failure strength of the preflawed specimen is approximately 50% of the triaxial compression strength of the intact specimen and about 90% of the UCS. The differences between the unloading failure strength and compression strength indicate that the compression strength obtained from laboratory quasi-static compression experiments cannot fully represent the peak failure strength for rock mass under excavation unloading condition. Therefore, it can be considered to use the unloading failure strength obtained from a quasi-static unloading test to evaluate the failure strength properties of underground engineering rock.

4.2. Unloading Damage Thresholds of Preflawned Specimens.

In fact, fracturing of the rock specimen is a complex process and simply measuring the peak stress does not capture this fracturing process [39]. In order to capture some unique features in the fracturing process, i.e., crack initiation, onset of fracture localization, and collapse peak, some damage thresholds are pointed out. The fracturing process of rock specimens can be recorded by many different ways, such as acoustic emission measurements and high-speed photography. In laboratory compression experiments, previous scholars determine the damage initiation and interaction thresholds for brittle rock based on the acoustic emissions [40, 41]. In the present study, the crack accumulation amount was used to reflect the fracturing process, and the damage thresholds of specimens under unloading condition were identified by the variation of the crack

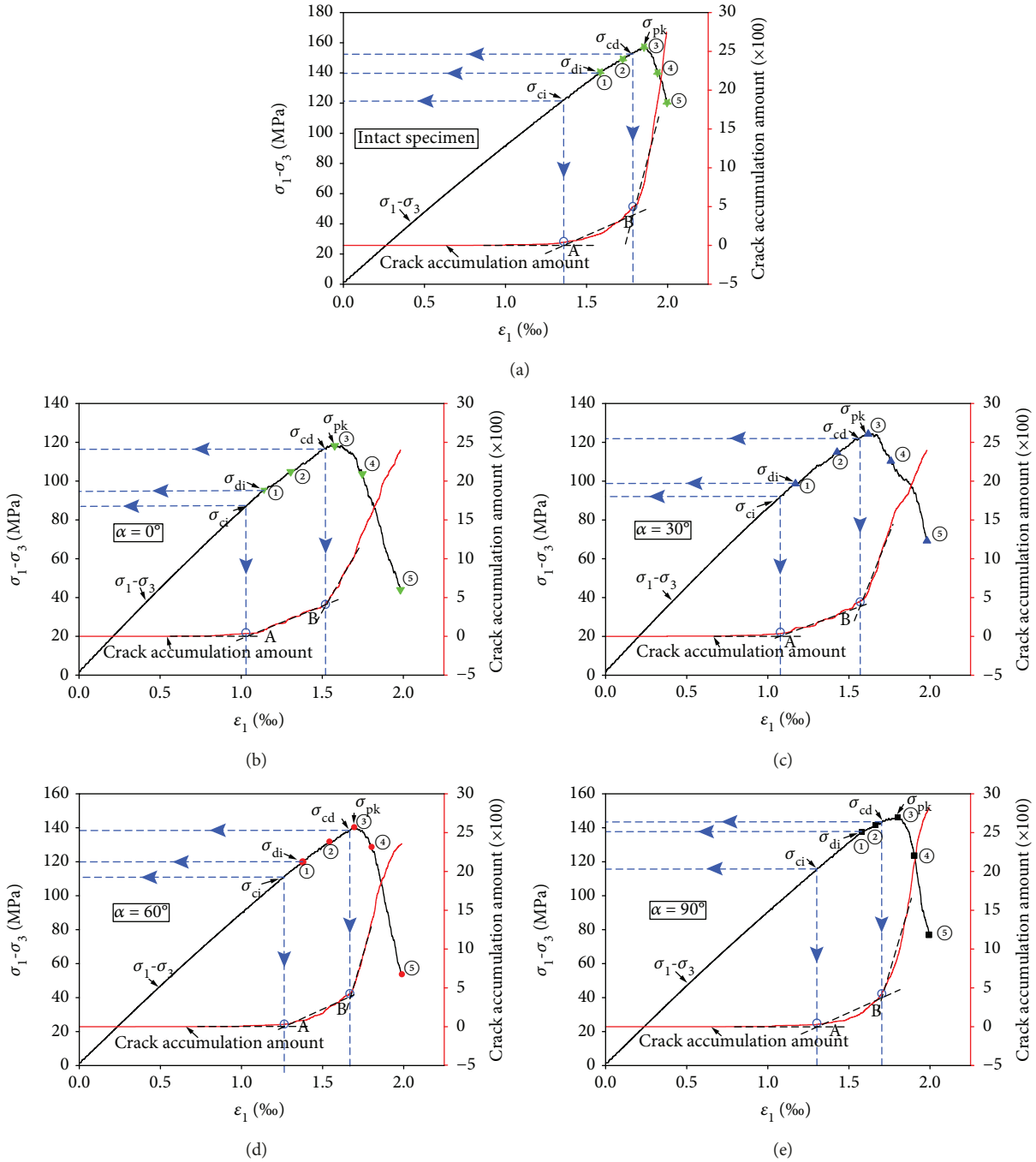


FIGURE 12: Relations among the deviatoric stress, crack accumulation, and strain of specimens under unloading condition.

accumulation amount. Figure 12 gives the relations of the deviatoric stress, the crack accumulation, and the associated axial strain response of specimens under unloading conditions. It can be seen that there are two critical points on the crack accumulation curves, i.e., point A and point B. Point A denotes the first intersection of two tangent lines in the crack accumulation curve, which can mark the onset of a slight increase in cracks. Point B denotes the second intersection of two tangent lines in the crack accumulation curve, which can mark the onset of a sharp increase in cracks. Cracks increase in a stable manner between points A and B,

while cracks begin to increase in an unstable manner after point B. The corresponding stress at point A is denoted as σ_{ci} , which represents the threshold stress for stable crack initiation. The stress at point B is denoted as σ_{cd} , which is a threshold stress for unstable crack development. Moreover, the other critical point was the point where the first observable macrocrack appears in the specimen [42]. In this study, the stress where the first observable macrocrack appears is defined as the other threshold, i.e., the damage initiation stress σ_{di} . The three damage thresholds (σ_{ci} , σ_{cd} , and σ_{di}) for different specimens are presented in Figure 12. It can

be found that $\sigma_{ci} > \sigma_{di} > \sigma_{cd} > \sigma_{pk}$ and σ_{pk} is the peak deviatoric stress.

For preflawed specimens, the damage threshold ratios are plotted against the flaw inclination angle (Figure 13). It can be seen in Figure 13 that the ratios of σ_{ci} , σ_{di} , and σ_{cd} to the peak deviatoric stress σ_{pk} are approximately 0.75, 0.85, and 0.97, respectively. According to previous studies, for the intact rock specimen under uniaxial compression, the crack initiation stress typically ranges from 0.3-0.5 UCS, and the unstable crack development stress is approximately 0.7-0.9 UCS [43]. It can be found that the damage threshold ratios of numerical preflawed rock specimens in the unloading tests are higher than those of real intact rock specimens in the uniaxial compression tests. This is because compared with the uniaxial compression test, the lateral stress in the unloading test constrains the initiation of cracks. In addition, the numerical rock specimen is composed of rigid particles, while the real rock specimen usually contains natural microfractures. As shown in Figure 13, the ratios of the stable crack initiation stress (σ_{ci}) and damage initiation stress (σ_{di}) rise with the increase in the flaw inclination angle, while the ratios of (σ_{cd}) change little with the increase in the flaw inclination angle. It indicates that the crack initiation stress is sensitive to the flaw inclination angle, and the preflawed specimen with a smaller flaw inclination angle is more prone to induce cracks under unloading condition. On the contrary, the stress of unstable crack development has no clear trend with the variation of the flaw inclination angle.

4.3. Cracking Characteristics of Preflawned Specimens under Unloading Condition. The cracking characteristics of preflawned specimens at any moment under unloading condition, including crack distribution, crack extension, and crack amount, can be recorded in numerical simulations. To analyze the cracking characteristics in detail, Figure 14 shows the crack distributions in the specimens at some specific points during the unloading process. These specific points are denoted by numbers which correspond to the points in stress-strain curves in Figure 12. For example, point ① refers to the damage initiation stress in the stress-strain curve. Point ② corresponds to a stress before the peak deviatoric stress, and the crack count at point ② is approximately 50% of the crack count at the peak deviatoric stress (point ③). Point ④ is a stress after the peak deviatoric stress, and the crack count at point ④ is approximately 2.5 times the crack count at the peak deviatoric stress. Point ⑤ is the stress at the end of unloading.

As shown in Figure 14, the cracking distribution and crack extension for different specimens under unloading condition are obviously different. To make it clearer, the cracking process was divided into two stages, i.e., stage I—prior to the peak deviatoric stress (including the peak deviatoric stress, ①, ②, and ③)—and stage II—after the peak deviatoric stress (④ and ⑤).

In stage I, the specimens undergo the elastic deformation and the crack initiation and propagation before reaching the peak deviatoric stress. For the intact specimen, the cracks distribute randomly in the specimen, while for the preflawned specimen with an inclined angle of 0° , cracks intensively

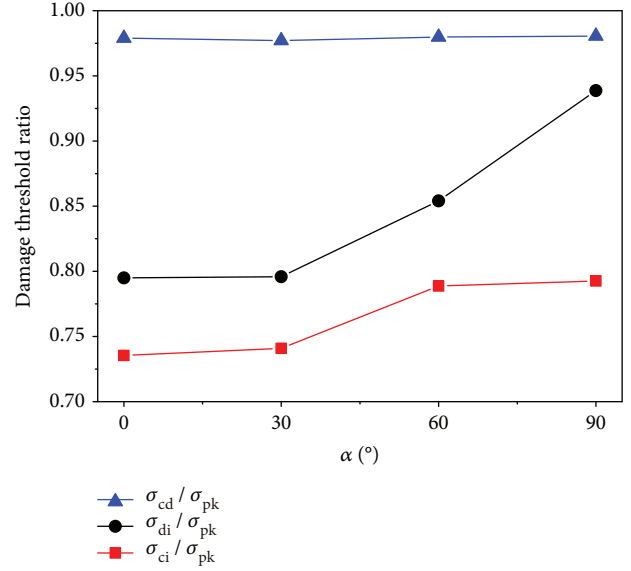


FIGURE 13: Damage threshold ratios of preflawned specimens under unloading condition.

distribute around the flaw tips and flaw surfaces. This phenomenon verifies the results of stress state analyses for preflaws based on Figure 10 and equation (11). At an inclined angle of 0° , the normal stress on the flaw is large enough, making the cracks to easily initiate and propagate around the flaw. For the preflawned specimen with an inclined angle of 30° , cracks mainly initiate and extend along the flaws tips. For the preflawned specimen at an inclined angle of 60° , cracks mainly distribute at the area of flaw inner tips and make a direct coalescence between the two preflaws. For the preflawned specimen with an inclined angle of 90° , a small number of cracks accumulate around the flaws, while many cracks distribute randomly in the specimens. This phenomenon verifies that the crack initiation of this specimen is less affected by the flaws.

In stage II, for the intact specimen, the accumulation of cracks shows as discrete shear planes, which is totally different from the failure modes of the intact specimen under compression condition. For the preflawned specimen with an inclined angle of 0° , cracks continually extend from the flaw tips and flaw surfaces. The cracks at the inner tips form a "V"-shaped indirect coalescence between the two preflaws. For the preflawned specimen with an inclined angle of 30° , the cracks at the inner tip of the left flaw extend downwards while those at the inner tip of the right flaw extend upwards; therefore, there is no coalescence between the two preflaws. For the preflawned specimen with an inclined angle of 60° , the cracks which extend along the flaw tips make the specimen fail at a shear failure plane. For the preflawned specimen with an inclined angle of 90° , the two preflaws do not exhibit coalescence, and very little cracks accumulate around the preflaws. By comparing the ultimate failure modes of specimens at point ⑤, it can be found that for preflawned specimens with an inclined angle of 0° and 30° , there are a lot of axial splitting cracks (marked by dashed lines in Figure 14), and for preflawned specimens with an inclined angle of 60°

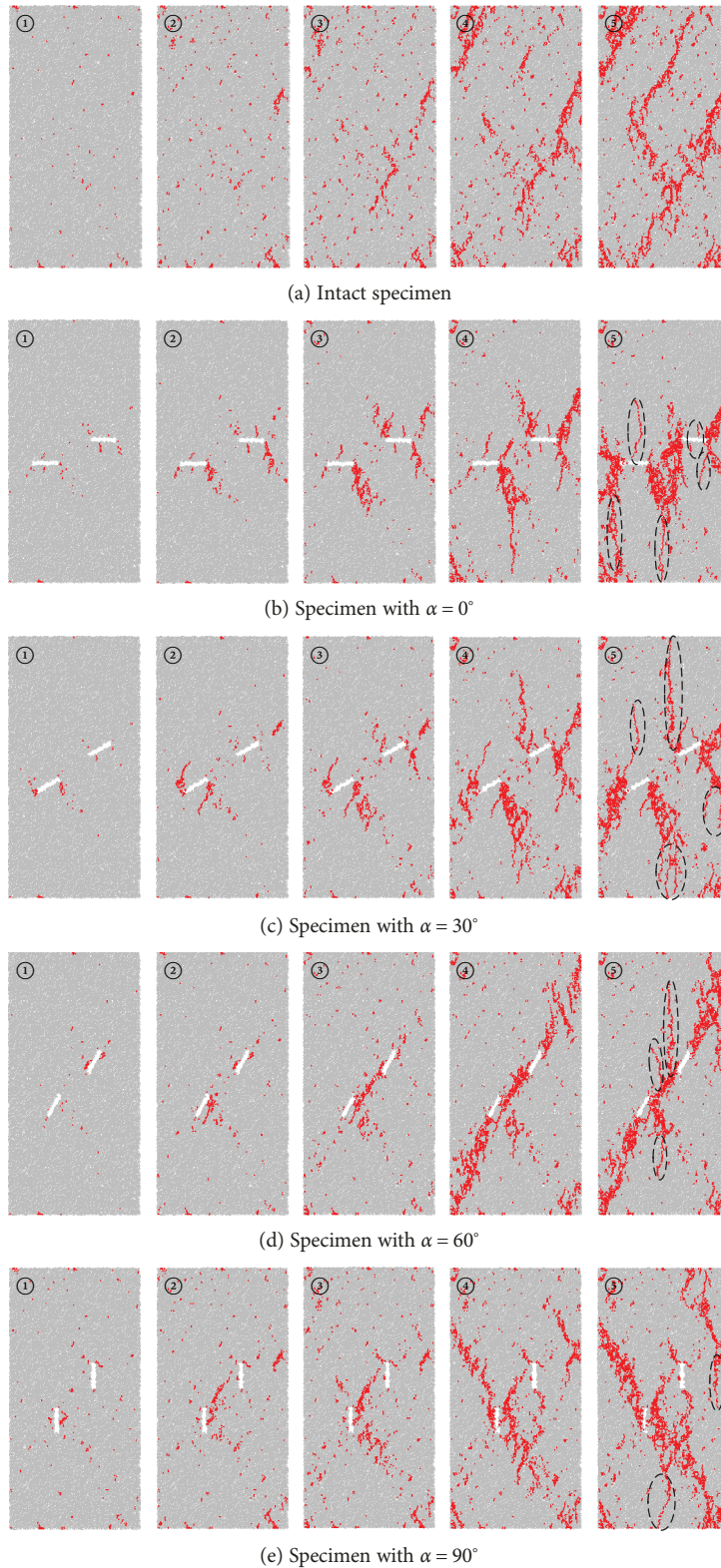


FIGURE 14: Cracking process of specimens under unloading condition (the red short lines in numerical specimens represent microcracks).

and 90° , the axial splitting cracks are little. Meanwhile, there are nonsplitting cracks in the intact specimen. Moreover, at the end of unloading (point ⑤), the ultimate crack amounts

of the intact specimen and preflawed specimens with inclined angles of 0° , 30° , 60° , and 90° are 2747, 2402, 2395, 2356, and 2826, respectively. It indicates that the ultimate crack amount

in specimens does not show a strong correlation with the flaws. This is possibly because two preflaws are not enough to make a significant difference in the crack amount for the preflawed specimen. If more flaws (or flaw networks) are created at a smaller inclination angle (such as 0° or 30°), then more cracks would initiate and propagate around the flaws, which may significantly influence the crack amount of the preflawed specimen under the unloading condition.

5. Conclusions

Based on the unloading stress condition of hard rock in underground excavation, numerical simulations were performed to analyze the unloading responses of marble specimens containing preflaws under unloading condition. The unloading strength properties, damage thresholds, and cracking characteristics of preflawed specimens with different flaw inclination angles were deeply investigated. The following conclusions can be summarized:

- (1) The unloading failure strength of a specimen containing two preflaws decreases by 5.5%-20% compared to that of the intact specimen. With the increase in the flaw inclination angle, the unloading failure strength of a specimen containing two preflaws exhibits an "S"-shaped increasing trend
- (2) Three damage thresholds (σ_{ci} , σ_{di} , and σ_{cd}) are determined based on the crack accumulation of specimens under unloading condition. For preflawed specimens, the damage threshold ratios of σ_{ci} and σ_{di} rise with the increase in the flaw inclination angle, while the damage threshold ratio of σ_{cd} has no clear change trend with the variation of the flaw inclination angle
- (3) Prior to the peak deviatoric stress, the cracks of preflawed specimens are distributed in a centralized manner around the flaw tips and flaw surfaces when the flaw inclination angle is smaller, while the distribution of the cracks for the intact specimen and preflawed specimen with $\alpha = 90^\circ$ is decentralized. After the peak deviatoric stress, the coalescence form between two flaws varies with the change of the flaw inclination angle. Moreover, at the end of unloading, there are obvious axial splitting cracks for preflawed specimens with $\alpha = 0^\circ$ and 30° , while axial splitting cracks are little in the preflawed specimen with $\alpha = 60^\circ$ and 90° and completely none in the intact specimen

These conclusive remarks can provide useful information for underground mechanical excavation. For one thing, the unloading failure strength defined in this study can be considered a parameter to evaluate the actual failure strength properties of rock mass in a mechanical excavation process. For another, the findings show that inducing flaws can reliably reduce the unloading failure strength and promote crack initiation and propagation of hard rock during the unloading process. Thus, inducing preflaws in hard rock will benefit the underground

mechanical excavation. In particular, when inducing preflaws at a smaller flaw inclination angle, the unloading failure and crack initiation are more likely to happen, and this means that inducing preflaws with a smaller inclination angle (e.g., vertical to the unloading direction) will be more helpful to improve the excavation efficiency.

Data Availability

The data used to support the findings of this study are available from the corresponding author upon request.

Conflicts of Interest

The authors declare that they have no conflicts of interest.

Acknowledgments

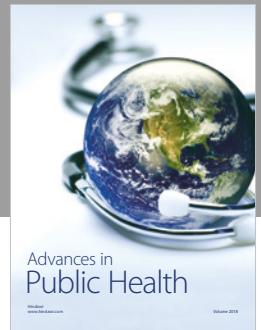
The work described in this paper was supported by the National Nature Science Foundation of China (nos. 41630642 and 11472311) for which the authors are very thankful.

References

- [1] J. B. Martino and N. A. Chandler, "Excavation-induced damage studies at the underground research laboratory," *International Journal of Rock Mechanics and Mining Sciences*, vol. 41, no. 8, pp. 1413–1426, 2004.
- [2] T. D. Rathnaweera, P. G. Ranjith, X. Gu et al., "Experimental investigation of thermomechanical behaviour of clay-rich sandstone at extreme temperatures followed by cooling treatments," *International Journal of Rock Mechanics and Mining Sciences*, vol. 107, pp. 208–223, 2018.
- [3] W. Wang, H. Wang, D. Li, H. Li, and Z. Liu, "Strength and failure characteristics of natural and water-saturated coal specimens under static and dynamic loads," *Shock and Vibration*, vol. 2018, Article ID 3526121, 15 pages, 2018.
- [4] W. Lu, J. Yang, P. Yan et al., "Dynamic response of rock mass induced by the transient release of in-situ stress," *International Journal of Rock Mechanics and Mining Sciences*, vol. 53, pp. 129–141, 2012.
- [5] L. Weng, L. Huang, A. Taheri, and X. Li, "Rockburst characteristics and numerical simulation based on a strain energy density index: a case study of a roadway in Linglong gold mine, China," *Tunnelling and Underground Space Technology*, vol. 69, pp. 223–232, 2017.
- [6] C. Li and X. Li, "Influence of wavelength-to-tunnel-diameter ratio on dynamic response of underground tunnels subjected to blasting loads," *International Journal of Rock Mechanics and Mining Sciences*, vol. 112, pp. 323–338, 2018.
- [7] L. Dong, D. Sun, X. Li, J. Ma, L. Zhang, and X. Tong, "Interval non-probabilistic reliability of surrounding jointed rockmass considering microseismic loads in mining tunnels," *Tunnelling and Underground Space Technology*, vol. 81, pp. 326–335, 2018.
- [8] P. Hartlieb, B. Grafe, T. Shepel, A. Malovyk, and B. Akbari, "Experimental study on artificially induced crack patterns and their consequences on mechanical excavation processes," *International Journal of Rock Mechanics and Mining Sciences*, vol. 100, pp. 160–169, 2017.

- [9] N. A. Sifferlinger, P. Hartlieb, and P. Moser, "The importance of research on alternative and hybrid rock extraction methods," *BHM berg- und Hüttenmännische Monatshefte*, vol. 162, no. 2, pp. 58–66, 2017.
- [10] N. Bilgin, T. Dincer, H. Copur, and M. Erdogan, "Some geological and geotechnical factors affecting the performance of a roadheader in an inclined tunnel," *Tunnelling and Underground Space Technology*, vol. 19, no. 6, pp. 629–636, 2004.
- [11] J. Rostami, "Performance prediction of hard rock tunnel boring machines (TBMs) in difficult ground," *Tunnelling and Underground Space Technology*, vol. 57, pp. 173–182, 2016.
- [12] F. J. Macias, P. D. Jakobsen, Y. Seo, and A. Bruland, "Influence of rock mass fracturing on the net penetration rates of hard rock TBMs," *Tunnelling and Underground Space Technology*, vol. 44, pp. 108–120, 2014.
- [13] S. Q. Yang and H. W. Jing, "Strength failure and crack coalescence behavior of brittle sandstone samples containing a single fissure under uniaxial compression," *International Journal of Fracture*, vol. 168, no. 2, pp. 227–250, 2011.
- [14] X. Li, H. Konietzky, and X. Li, "Numerical study on time dependent and time independent fracturing processes for brittle rocks," *Engineering Fracture Mechanics*, vol. 163, pp. 89–107, 2016.
- [15] X. P. Zhang, L. N. Y. Wong, and S. Wang, "Effects of the ratio of flaw size to specimen size on cracking behavior," *Bulletin of Engineering Geology and the Environment*, vol. 74, no. 1, pp. 181–193, 2015.
- [16] J. Bi, X. P. Zhou, and Q. H. Qian, "The 3D numerical simulation for the propagation process of multiple pre-existing flaws in rock-like materials subjected to biaxial compressive loads," *Rock Mechanics and Rock Engineering*, vol. 49, no. 5, pp. 1611–1627, 2016.
- [17] H. Lee and S. Jeon, "An experimental and numerical study of fracture coalescence in pre-cracked specimens under uniaxial compression," *International Journal of Solids and Structures*, vol. 48, no. 6, pp. 979–999, 2011.
- [18] X. Zhuang, J. Chun, and H. Zhu, "A comparative study on unfilled and filled crack propagation for rock-like brittle material," *Theoretical and Applied Fracture Mechanics*, vol. 72, pp. 110–120, 2014.
- [19] C. H. Park and A. Bobet, "Crack coalescence in specimens with open and closed flaws: a comparison," *International Journal of Rock Mechanics and Mining Sciences*, vol. 46, no. 5, pp. 819–829, 2009.
- [20] D. Huang, D. Gu, C. Yang, R. Huang, and G. Fu, "Investigation on mechanical behaviors of sandstone with two preexisting flaws under triaxial compression," *Rock Mechanics and Rock Engineering*, vol. 49, no. 2, pp. 375–399, 2016.
- [21] X. G. Zhao, J. Wang, M. Cai et al., "Influence of unloading rate on the strainburst characteristics of Beishan granite under true-triaxial unloading conditions," *Rock Mechanics and Rock Engineering*, vol. 47, no. 2, pp. 467–483, 2014.
- [22] D. Huang and Y. Li, "Conversion of strain energy in triaxial unloading tests on marble," *International Journal of Rock Mechanics and Mining Sciences*, vol. 66, pp. 160–168, 2014.
- [23] K. Du, M. Tao, X.-b. Li, and J. Zhou, "Experimental study of slabbing and rockburst induced by true-triaxial unloading and local dynamic disturbance," *Rock Mechanics and Rock Engineering*, vol. 49, no. 9, pp. 3437–3453, 2016.
- [24] F. Zhao and M. C. He, "Size effects on granite behavior under unloading rockburst test," *Bulletin of Engineering Geology and the Environment*, vol. 76, no. 3, pp. 1183–1197, 2017.
- [25] A. Manouchehriani and M. Cai, "Simulation of unstable rock failure under unloading conditions," *Canadian Geotechnical Journal*, vol. 53, no. 1, pp. 22–34, 2016.
- [26] J. Li, P. Fan, and M. Wang, "Failure behavior of highly stressed rocks under quasi-static and intensive unloading conditions," *Journal of Rock Mechanics and Geotechnical Engineering*, vol. 5, no. 4, pp. 287–293, 2013.
- [27] F. Du, G. Jiang, and Z. Chen, "A numerical simulation study of the migration law of water-sand two-phase flow in broken rock mass," *Geofluids*, vol. 2018, Article ID 6418476, 12 pages, 2018.
- [28] F. Wang, C. Duan, S. Tu, N. Liang, and Q. Bai, "Hydraulic support crushed mechanism for the shallow seam mining face under the roadway pillars of room mining goaf," *International Journal of Mining Science and Technology*, vol. 27, no. 5, pp. 853–860, 2017.
- [29] Y. Wu, Q. Liu, A. H. C. Chan, and H. Liu, "Implementation of a time-domain random-walk method into a discrete element method to simulate nuclide transport in fractured rock masses," *Geofluids*, vol. 2017, Article ID 5940380, 13 pages, 2017.
- [30] D. O. Potyondy and P. A. Cundall, "A bonded-particle model for rock," *International Journal of Rock Mechanics and Mining Sciences*, vol. 41, no. 8, pp. 1329–1364, 2004.
- [31] A. Fakhimi, "Application of slightly overlapped circular particles assembly in numerical simulation of rocks with high friction angles," *Engineering Geology*, vol. 74, no. 1–2, pp. 129–138, 2004.
- [32] N. Cho, C. D. Martin, and D. C. Segol, "A clumped particle model for rock," *International Journal of Rock Mechanics and Mining Sciences*, vol. 44, no. 7, pp. 997–1010, 2007.
- [33] B. H. G. Brady and E. T. Brown, *Rock Mechanics for Underground Mining*, Springer, 2006.
- [34] R. Ulusay, *The ISRM Suggested Methods for Rock Characterization, Testing and Monitoring: 2007–2014*, Springer International Publishing, 2015.
- [35] W. C. Zhu, J. Wei, J. Zhao, and L. L. Niu, "2D numerical simulation on excavation damaged zone induced by dynamic stress redistribution," *Tunnelling and Underground Space Technology*, vol. 43, pp. 315–326, 2014.
- [36] X. Li, W. Cao, Z. Zhou, and Y. Zou, "Influence of stress path on excavation unloading response," *Tunnelling and Underground Space Technology*, vol. 42, pp. 237–246, 2014.
- [37] S. Q. Yang, W. L. Tian, Y. H. Huang, Z. G. Ma, L. F. Fan, and Z. J. Wu, "Experimental and discrete element modeling on cracking behavior of sandstone containing a single oval flaw under uniaxial compression," *Engineering Fracture Mechanics*, vol. 194, pp. 154–174, 2018.
- [38] T. Liu, B. Lin, Q. Zou, C. Zhu, and F. Yan, "Mechanical behaviors and failure processes of precracked specimens under uniaxial compression: a perspective from microscopic displacement patterns," *Tectonophysics*, vol. 672–673, pp. 104–120, 2016.
- [39] E. Hoek and C. D. Martin, "Fracture initiation and propagation in intact rock – a review," *Journal of Rock Mechanics and Geotechnical Engineering*, vol. 6, no. 4, pp. 287–300, 2014.

- [40] E. Eberhardt, D. Stead, B. Stimpson, and R. S. Read, "Identifying crack initiation and propagation thresholds in brittle rock," *Canadian Geotechnical Journal*, vol. 35, no. 2, pp. 222–233, 1998.
- [41] D. Li, C. C. Li, and X. Li, "Influence of sample height-to-width ratios on failure mode for rectangular prism samples of hard rock loaded in uniaxial compression," *Rock Mechanics and Rock Engineering*, vol. 44, no. 3, pp. 253–267, 2011.
- [42] X. P. Zhang and L. N. Y. Wong, "Cracking processes in rock-like material containing a single flaw under uniaxial compression: a numerical study based on parallel bonded-particle model approach," *Rock Mechanics and Rock Engineering*, vol. 45, no. 5, pp. 711–737, 2012.
- [43] C. D. Martin and N. A. Chandler, "The progressive fracture of Lac du Bonnet granite," *International Journal of Rock Mechanics and Mining Sciences & Geomechanics Abstracts*, vol. 31, no. 6, pp. 643–659, 1994.



Hindawi

Submit your manuscripts at
www.hindawi.com

